Bibliography

[1] Aim@Shape model repository. URL `http://shapes.aim-at-shape.net/`.

[2] Amira 5.0. URL `http://www.amira.com/`.

[3] FEBio finite elements for biomechanics software. URL `http://mrl.sci.utah.edu/software/febio`.

[4] INRIA model repository. URL `http://www-roc.inria.fr/gamma/download/download.php`.

[5] MESQUITE mesh quality improvement toolkit. URL `http://www.cs.sandia.gov/optimization/knupp/Mesquite.html`.

[6] PostView finite element post-processing software. URL `http://mrl.sci.utah.edu/software/postview`.

[7] PreView finite element pre-processing software. URL `http://mrl.sci.utah.edu/software/preview`.

[8] Python. URL `http://docs.python.org/`.

[9] TetGen. URL `http://tetgen.berlios.de/`.

[10] VRMesh Studio. URL `http://www.vrmesh.com/products/studio.asp`.

[11] SciPy: Open source scientific tools for python, 2001. URL `http://www.scipy.org/`.

[12] L. Aiello and C. Dean. *An introduction to human evolutionary anatomy*, Volume 1990. Academic Press, London.

[13] P.J. Besl and H.D. McKay. A method for registration of 3D shapes. *IEEE Transactions on Pattern Analysis and Machine Intelligence*, 14:239–256, 1992.

[14] A. Bjork. Some biological aspects of prognathism and occlusion of the teeth. *Acta Odontologica Scandinavica*, 9:3–27, 1950.

[15] N.G. Blanksma and T.M.G.J. van Eijden. Electromographic heterogeneity in the human temporalis muscle. *Journal of Dental Research*, 69:1686–1690, 1990.

[16] N.G. Blanksma, T.M.G.J. van Eijden, L.J. van Ruijven, and W.A. Weijs. Electromographic heterogeneity in the human temporalis and masseter muscles during dynamic task guided by visual feedback. *Journal of Dental Research*, 76:542–551, 1997.

[17] A. Boryor, M. Geiger, A. Hohmann, A. Wunderlich, C. Sander, F.M. Sander, and F.G. Sander. Stress distribution and displacement analysis during an intermaxillary disjunction - a three-dimensional fem study of a human skull. *Journal of Biomechanics*, 41:376–382, 2008.

[18] P. Brown and T. Maedea. Post-pleistocene diachromic change in east asian facial skeletons: shape and volume of the orbits. *Anthropological Science*, 112: 29–40, 2004.

[19] R. Bryan, P.S. Mohan, A. Hopkins, F. Galloway, M. Taylor, and P.N. Nair. Statistical modelling of the whole human femur incorporating geometric and material properties. *Mechanical Engineering and Physics*, 32:57–65, 2010.

[20] D.L.A. Camacho, R.H. Hopper, G.M. Lin, and B.S. Myers. An improved method for finite element mesh generation of geometrically complex structures with application to the skullbase. *Journal of Biomechanics*, 30:1067–1070, 1997.

[21] W. Che, J. Paul, and X. Zhang. Lines of curvature and umbilical points for implicit surfaces. *Computer Aided Geometric Design*, 24:395–409, 2007.

[22] H. Chen and B. Bhanu. 3D free-form object recognition in range images using local surface patches. *Pattern Recognition Letters*, 28:1252–1262, 2007.

[23] S.N. Cobb and P. O'Higgins. Homonins do not share a common postnatal facial ontogenetic shape trajectory. *Journal of Experimental Zoology*, 302B:302–321, 2004.

[24] R.D. Cook, D.S. Malkus, M.E. Plesha, and R.J. Witt. *Concepts and applications of Finite Element Analysis*. John Wiley & Sons, 2002.

[25] N. Curtis, K. Kupczik, P. O'Higgins, M. Moazen, and M. Fagan. Predicting skull loading: Applying multibody dynamics analysis to a macaque skull. *The Anatomical Record*, 291:491–501, 2008.

[26] A. de Boer, M.S. van der Schoot, and H. Bijl. Mesh deformation based on radial basis function interpolation. *Computers and Structures*, 85:784–795, 2007.

[27] E.P. Degarmo, J.T. Black, and R.A. Kohser. *Materials and Processes in Manufacturing*. Wiley, 9th edition, 2003.

[28] S. Du, N. Zheng, S. Ying, and J. Liu. Affine iterative closest point algorithm for point sets registration. *Pattern Recognition Letters*, 31:791–799, 2010.

[29] J.M. Escobar, E. Rodrigues, R. Montenegro, G. Montero, and J.M. Gonzalez-Yuste. Simultaneous untangling and smoothing of tetrahedral meshes. *Computer Methods in Applied Mechanics and Engineering*, 192:2775–2787, 2003.

[30] M.J. Fehrenbach and S.W. Herring. *Illustrated Anatomy of the Head and Neck*. W.B. Saunders Company, Philadelphia, 1996.

[31] A. Frome, D. Huber, R. Kolluri, T. Bulow, and J. Malik. Recognizing objects in range data using regional point descriptors. In *European Conference on Computer Vision*, volume 3, pages 224–237, 2004.

[32] F. Groning, J. Liu, M.J. Fagan, and P. O'Higgins. Validating a voxel based finite element model of a human mandible using digital speckle patter interferometry. *Journal of Biomechanics*, 42:1224–1229, 2009.

[33] K. Hildebrandt, K. Polthier, and M. Wardetzky. Smooth feature lines on surface meshes. *Eurographics Symposium on Geometric Processing*, 2005.

[34] A. Hsieh, C. Ho, and K. Fan. An extention of the bipartite weighted matching problem. *Pattern Recognition Letters*, 16:347–353, 1995.

[35] I. Ichim, M. Sawin, and J.A. Kieser. Mandibular biomechanics and development of the human chin. *Journal of Dental Research*, 85:638–642, 2006.

[36] I.T. Jolliffe. *Principal Component Analysis, Second Edition*. Springer, 2002.

[37] S. Kim and C. Kim. Finding ridges and valleys in a discrete surface using a modified mls approximation. *Computer Aided Design*, 38:173–180, 2006.

[38] K. Kupczik, C.A. Dobson, M.J. Fagan, R.H. Crompton, C.E. Oxnard, and P. O'Higgins. Assessing mechanical function of the zygomatic region in macaques: validation and sensitivity testing of finite element models. *Journal of Anatomy*, 210:41–53, 2007.

[39] E.N. L'Abbe, M. Loots, and M.J. Meiring. The pretoria bone collection: A modern south african skeletal sample *Documented Collection*, The University of Pretoria, 2005.

[40] M. Meyer, M. Desbrun, P. Shröder, and A.H. Barr. Discrete differential-geometry operators for triangulated 2-manifolds. *Visualisation and Mathematics III*, 35–57, 2003.

[41] K. Miller, K. Chinzei, G. Orssengo, and P. Bednarz. Mechanical properties of brain tissue in-vivo: experiment and computer simulation. *Journal of Biomechanics*, 33:1369–1376, 2000.

[42] P. Mitteroecker and P. Gunz. Advances in geometric morphometrics. *Evolutionary Biology*, 36:235–247, 2009.

[43] P.M. Moore-Jansen, S.D. Ousley, and R.L. Jantz. Data collection procedures for forensics skeletal material: Report of investigations. Technical Report 48, The University of Tennessee: Department of Anthropology, Knoxville, 1994.

[44] M. Moshfeghi, S. Ranganath, and K. Nawyn. Three-dimensional elastic matching of volumes. *IEEE Transactions on Image Processing*, 3:128–138, 1994.

[45] Y. Ohtake, A. Belyaev, and H. Seidel. Ridge-valley lines on meshes via implicit surface fitting. *ACM Transactions on Graphics*, 23:609–612, 2004.

[46] J. Paphangkorakit and J.W. Osborn. Effects of human maximum bite force of biting on a softer or harder object. *Archives of Oral Biology*, 43:833–839, 1998.

[47] J. Peterson and P.C. Dechow. Material properties of the human cranial vault and zygoma. *The Anatomical Record Part A*, 274 A:785–97, 2003.

[48] G. Pileicikiene and A. Surna. The masticatory system from a biomedical perspective: A review. *Baltic Dental and Maxillofacial Journal*, 6:81–84, 2004.

[49] H. Preuschoft and U. Witzel. Functional shape of the skull in verebrates: Which forces determine skull morphology in lower primates and ancestral synapsids. *The Anatomical Record Part A*, (283A):402–413, 2005.

[50] C. Provatidis, B. Georgiopoulos, A. Kotinas, and J.P. McDonald. On the fem modelling of craniofacial changes during rapid maxillary expansion. *Medical Engineering and Physics*, 29:566–579, 2007.

[51] A. Quarterioni and S. Fausto. *Scientific Computing with MATLAB and Octave*. Springer, 2006.

[52] B.G. Richmond, B.W. Wright, I. Grosse, P.C. Dechow, F.R. Callum, M.A. Spencer, and D.S. Strait. Finite element analysis in functional morphology. *The Anatomical Record Part A*, 283A:259–274, 2005.

[53] J.H. Robertson. More on skeletal analysis and the race concept. *Current Anthropology*, 20:617, 1979.

[54] D.E. Slice. Geometric morphometrics. *Annual Review in Anthropology*, 36: 261–281, 2007.

[55] H.F. Smith, C.E. Terhune, and C.A. Lockwood. Genetic, geographic and environmental correlates of human temporal bone variation. *American Journal of Physical Anthropology*, 134:312–322, 2007.

[56] J.B. Smith and C.W. Snuggs. Dynamic properties of the human head. *Journal of Sound and Vibration*, 48:35–43, 1976.

[57] D.S. Strait, B.G. Richmond, M.A. Spencer, F.R. Callum, P.C. Dechow, and B.A. Wood. Masticatory biometrics and its relevance to early hominid phylogeny: An examination of palatal thickness using finite-element analysis. *Journal of Human Evolution*, 52:585–599, 2007.

[58] D.S. Strait, Q. Wang, P.C. Dechow, F.R. Callum, B.G. Richmond, M.A. Spencer, and B.A. Patel. Modeling elastic properties in finite element analysis: how much precision is needed to produce an accurate model? *The Anatomical Record Part A*, 283A:275–287, 2005.

[59] G. Subsol, J.P. Thirion, and N. Ayache. A general scheme for automatically building 3D morphometric anatomical atlasses: application to a skull atlas. *Medical Image Analysis*, 2:37–60, 1998.

[60] K. Tanne, J. Miyasaka, Y. Yamagata, R. Sachdeva, and S. Tsutsumi. Three-dimensional model of the human craniofacial skeleton: method and preliminary results using finite element analysis. *Journal of Biomedical Engineering*, 10: 246–252, 1988.

[61] G. Taubin. A signal processing approach to fair surface design. In *Proceedings of the 22nd Annual Conference on Computer Graphics and Interactive Techniques*, pages 351–358, 1995.

[62] J. Vollmer, R. Mencl, and H. Müller. Improved laplacian smoothing of noisy surface meshes. *Eurographics*, 18:131–138, 1999.

[63] S.H.Y. Wei. Craniofacial variations, sex differences and the nature of prognathism in chinese subjects. *Angle Orthodontist*, 39:303–315, 1969.

[64] W.A. Weijs and B. Hillen. Cross-sectional areas and estimated intrinsic strength of the human jaw muscles. *Acta Morphol Neerl-Scand*, 23:267–274, 1985.

[65] J.A. Weiss, B.N. Maker, and S. Govindjee. Finite element implementation of incompressible, transversely isotropic hyperelasticity. *Computer Methods in Applied Mechanics and Engineering*, 135:107–128, 1996.

[66] T.D. White. *Human Osteology*. Academic Press, San Diego, California, 2000.

[67] S. Wroe, K. Moreno, P. Clausen, C. Mchenry, and D. Curnoe. High-resolution three dimensional computer simulation of homonid cranial mechanics. *The Anatomical Record*, 290:1248–1255, 2007.

[68] D. Xiao, D. Zahra, P. Bourgeat, P. Berghofer, O.A. Tamayo, C. Wimberley, M.C. Gregoire, and O. Salvado. An improved 3d shape context based non-rigid registration method and its application to small animal skeletons registration. *Computerized Medical Imaging and Graphics*, 34:321–332, 2010.

[69] J. Xie, P. Heng, and M. Shah. Shape matching and modeling using skeletal context. *Pattern Recognition*, 41:1756–1767, 2008.

[70] S. Yoshizawa, A. Belyaev, H. Yokota, and H. Seidel. Fast, robust, and faithful methods for detecting crest lines on meshes. *Computer Aided Geometric Design*, 25:545–560, 2008.

[71] Z. Yu, M. J. Holst, and A. McCammon. High-fidelity geometric modeling for biomedical applications. *Finite Elements in Analysis and Design*, 44:715–723, 2008.

Appendix A

Finite Element Analysis on a Prognathic and Orthognathic Skull Geometry

A.1 Introduction

The forces applied through the cycles of mastication are influenced by a variety of factors. The size and strength of masticatory muscles and their attachment to structures within the crania are of importance. The size and form of these cranial structures and the location of healthy teeth and gums also have a major influence.

To simulate mastication and determine the corresponding stress field, a finite element model can be created and analysed from a digital patient's cranial geometry. This includes decisions as to the appropriate material properties, boundary conditions and imposed loads.

The background work to this project aimed at applying the general rules of bone behavior and muscle activity in order to test a hypothesis about a single facial characteristic. This is done in collaboration with a Ph.D. student in Anthropology. The hypothesis of the Ph.D. work states that the location of bone stress in the crania of a prognathic[1] facial form will vary from that in the orthognathic[2] facial form. With this in mind, the hypothesis is tested with the aid of a finite element tool.

[1] One or both jaws projecting forward.
[2] Jaws don't project forward giving a flatter facial profile.

Chapter 2 in this report covers most of the ideas and background work done to test the hypothesis. This appendix is included to accompany Chapter 2 and serves as additional documentation of the initial FEA. Although much of this appendix is duplicated from Chapter 2, imposed boundary conditions are covered more accurately and additional results are displayed.

A.2 Geometries

The reason for this study is a validation on the the adaption of skull form to minimise internal stress due to mastication. For this reason two skulls were selected for analysis based on gnathic index and sufficient dentition from the University of Pretoria skull collection [39]. A skull with a gnathic index of 106.9 is used to represent a prognathic facial form and a skull with a gnathic index of 91.5 represents the orthognathic facial form.

A.2.1 Model Creation

A Siemens SOMATOM 16 medical computer tomography (CT) scanner was used to create scans of the selected geometries. 629 slices was made of the prognathic skull and 656 of the orthognathic skull with a set scanner thickness of 0.75 mm. Using these scans as image stacks imported into Amira® 5.0 [2], a triangulated surface mesh was extracted. This is done after a thresholding procedure where adjustments are made on the gray scale of voxel density data. Attenuation of the scans highlights bony morphology while eliminating unwanted material picked up by the scanner.

Intersecting and inconsistent triangles as well as the effects of postmortem trauma and decay has to be taken into account. For this reason the extracted surface representations are then edited and smoothed using VRMesh Studio [10]. Taking into account that exact stress values aren't required and this study is mainly on the variation in stress pattern, a four noded tetrahedral finite element mesh is created from the final surface representation using TetGen [9]. This results in a model for the prognathic skull consisting of 113 104 nodes and 401 455 elements while 110 645 nodes and 397 354 elements are used in representing the orthognathic skull in the initial analysis.

A.3 Material Properties

Significant variation in material properties have been documented for a range of different bones and within different areas of the same bone structure. The anisotropic nature of bone and how to model it is however not the focus of this research. It is assumed that comparing only the stress fields produced by mastication doesn't require the accurate simulation of bone to the extent that exact stress and strain values are recovered from a finite element analysis.

For similar analyses done in literature, isotropic bone material properties have been found capable of producing realistic stress patterns [17, 20, 32, 35, 38, 60]. Considering the highly reduced level of effort this entails the same assumption was made to model the full skull and teeth with a single linear elastic material.

Tetrahedral finite element meshes are imported into PreView [7] to set up the model by defining material properties and boundary conditions. The Young's modulus and Poisson's ratio used was taken from the literature [17, 20, 32, 35, 38, 50, 60] to be 16 GPa and 0.3 .

A.4 Boundary Conditions

FEBio [3], a solver developed specifically for biomechanics finite element applications is used in this study. Although this package allows muscles and tendons to be modelled using an array of element types it was decided that the forces of mastication would be modelled as external forces on the skull. The forces are applied to nodes in the region representing the approximate sites of muscle attachment as described with the help of Figure 2.1.

The average nodal coordinate value of nodes on the occipital condyles (OC) in the region of the foramen magnum is used as the origin of a Cartesian coordinate axis. Here the x-axis is directed from the right to the left, y-axis orientated anterior posterior (front to back) and the z-axis inferior superior (bottom to top) to the skull.

Muscle force values are first approximated for a vertical bite force on the first incisor and first molar. A system of equations is then set up to solve the bite force and reaction forces at the temporomandibular joint (TMJ) for each skull model before all forces are scaled, resulting in an identical force on the teeth. The skulls are scaled to have the same basion to nasion distance (See ba-n in Figure 1.1) and

		Temporalis	Superficial Masseter	Deep Head Masseter	Medial Pterygoid
(a)	**Working Side**				
	Force [N]	410	230	100	250
(b)	**Balancing Side**				
	% Working	41	47	36	20
	Force [N]	168.1	108.1	36	50

Table A.1: Initial muscle forces. (a) Working side force values used and (b) balancing side as a percentage of working side force derived from [57] with equivalent force value.

	Section	1	2	3	4	5	6	7
(a)	**Activity [%]**	86	70	56	52	44	47	49
(b)	**Nodes**							
	Prognathic L	57	28	25	32	20	9	15
	R	61	39	35	33	20	11	15
	Orthognathic L	62	32	37	28	22	13	17
	R	69	36	36	38	27	13	18
(c)	**Force per node [N]**							
	Prognathic L	3.22	2.62	2.10	1.95	1.65	1.76	1.83
	R	1.15	0.94	0.75	0.70	0.59	0.63	0.66
	Orthognathic L	2.87	2.34	1.87	1.74	1.47	1.57	1.64
	R	1.05	0.85	0.68	0.63	0.54	0.57	0.60

Table A.2: Temporalis muscle section force distribution. (a) Activity of muscle sections approximated from [15] for a vertical bite force. (b) Nodes in each section and (c) weighted resultant force value.

rotated so a line through the equivalent nodal coordinates of the TMJ would be exactly parallel to the x-axis.

A.4.1 Muscle Forces

Muscle action during the cycles of mastication are different for working and balancing sides. For this stress simulation the left side of the skull is arbitrarily chosen as the working side of the dental arcade where bite force is applied. Force values used here is determined from literature with force scaling factors obtained from a study on muscle activity during mastication [57].

The initial muscle forces used to calculate bite force and reaction forces at the TMJs are given in Table A.1. These forces along with balancing muscle forces

determined on the opposite side are tabulated.

For each skull, the muscle force directions are determined. This is done from the equivalent average nodal coordinate of nodes selected to represent the location of muscle attachment. A unit vector from this muscle origin to a digital landmark representing the approximate area of attachment on the mandible is then determined.

The temporalis muscle is divided into seven segments, numbered and ordered anterior to posterior. Figure 2.2 (a) shows the approximate positions of the segmentation of the fan like temporalis on the prognathic skull form with numbers 1 through 7. Segmenting this muscle enjoys frequent application for similar studies done in literature [52] and is motivated as follows:

- Temporalis muscle activity and thickness varies from anterior to posterior.
- The segments can act in different directions, representing the fan-like muscle with greater accuracy than a single force direction.

The force values for each segment is determined using the number of nodes in each section along with the approximate muscle activity in that section to give each segment a weight. The relative weight of a segment i is determined from

$$\omega_i = \frac{n_i \times EMG_i}{\sum_{j=1}^{N_{\text{seg}}} (n_j \times EMG_j)}, \tag{A.1}$$

where n is the number of nodes and EMG is the approximate electromyographic reading measured in that section of the muscle for an applied vertical bite force. This is approximated from work done by Blanksma and van Eijden [15]. This weight along with the known direction of force of each segment is used to then calculate the force each segment contributes. The contributions result in 410 N on the working side and 168.1 N on the balancing side positions where the temporalis attaches to the mandible. The muscle section activity, number of nodes in each section and forces applied to the nodes in each section of the temporalis muscle is presented in Table A.2.

The work done by Blanksma and van Eijden [15] does not specify whether temporalis section activity is different for prognathic or orthognathic facial form during an applied vertical bite force. It is assumed that their results may be used for both skull forms analysed.

A.4.2 Reaction Forces

The model is constrained in the region of the foramen magnum at the occipital condyles in all six degrees of freedom to prevent rigid body movement. The masticatory forces applied usually act on the mandible and so are an internal balanced system. A problem exists however in that only six unknowns can be solved for a statically determinate analysis in three dimensions while there are seven unknowns that require solution:

- One unknown for the z-value of the force at the tooth. The friction forces are not taken into account for this analysis so that the bite force is assumed to have a single component. This is also due to constraints on the number of unknowns that can be solved in a three dimensional statically determinate analysis.
- Six unknowns for the x- , y- and z-values for working and balancing side TMJ forces.

A simple free body diagram of the problem in the $y-z$ plane is visible in Figure A.1. Here the vector components in red represent the components of a muscle force. These are displayed as if applied to the average nodal coordinate of nodes chosen to represent the position of that muscle's attachment. The vector components in blue are the unknown balancing force components at the tooth and TMJs. By solving the system of Equations (A.2), the unknown balancing force values are obtained.

The skull is rotated so a line through the equivalent nodal coordinates of the TMJs is exactly parallel to the x-axis. The components of these forces in the x-direction can now be bundled, allowing a solvable system of equations where only 6 unknowns are present. Static force balance equations are used. The skull is assumed a rigid body that does not undergo any deformation during loading. From

$$\begin{aligned} \sum F &= 0 \\ \sum M_{\mathrm{OC}} &= 0 \end{aligned} \tag{A.2}$$

with F the vector of forces and M_{OC} the moments about the occipital condyles, the resulting system of equations is set up. The six equations that are solved can be

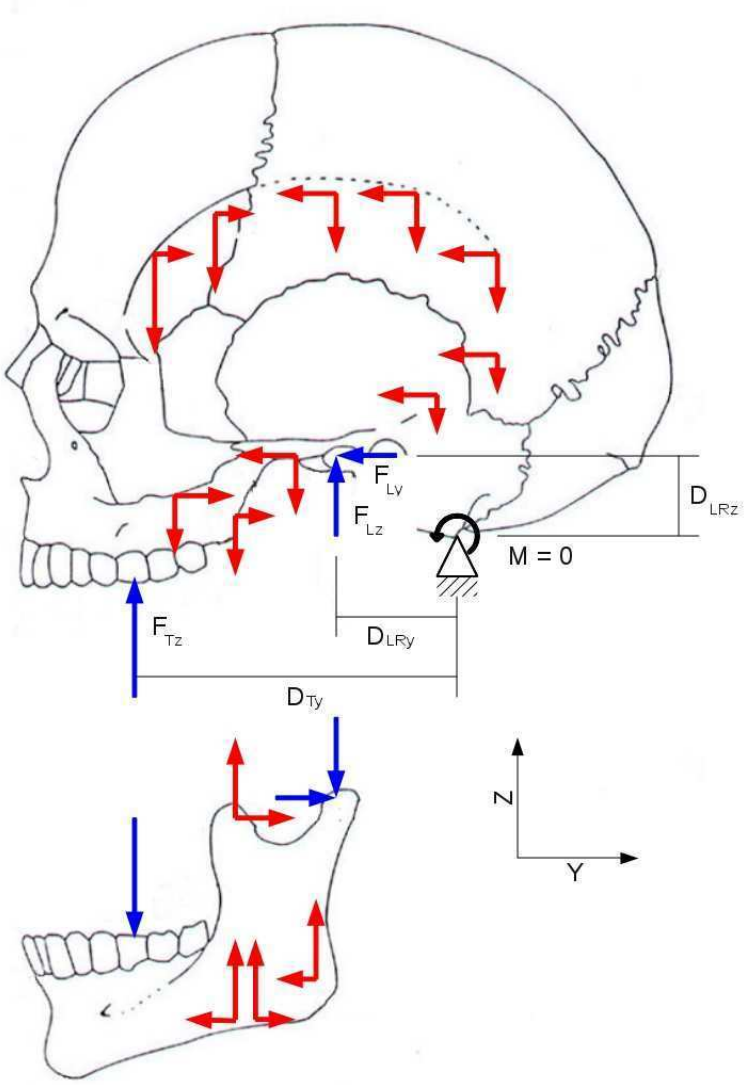

Figure A.1: Free body diagram of the skull in the yz-plane. Muscle force components are visible in their approximate locations (red) as well the reaction forces (blue) for the working side of both the crania and mandible .

given in the form

$$\begin{Bmatrix} \sum F_x \\ \sum F_y \\ \sum F_z \\ \sum M_{\mathrm{OC}x} \\ \sum M_{\mathrm{OC}y} \\ \sum M_{\mathrm{OC}z} \end{Bmatrix}_{\text{unknown}} = - \begin{Bmatrix} \sum F_x \\ \sum F_y \\ \sum F_z \\ \sum M_{\mathrm{OC}x} \\ \sum M_{\mathrm{OC}y} \\ \sum M_{\mathrm{OC}z} \end{Bmatrix}_{\text{known}} . \tag{A.3}$$

Using a free body diagram as in Figure A.1 along with all of the assumptions made, the system is then set up as

$$\begin{bmatrix} 1 & 0 & 0 & 0 & 0 & 0 \\ 0 & 1 & 1 & 0 & 0 & 0 \\ 0 & 0 & 0 & 1 & 1 & 1 \\ 0 & -D_{Lz} & -D_{Rz} & D_{Ly} & D_{Ry} & D_{Ty} \\ D_{LRz} & 0 & 0 & -D_{Lx} & -D_{Rx} & -D_{Tx} \\ -D_{LRy} & D_{Lx} & D_{Rx} & 0 & 0 & 0 \end{bmatrix} \begin{Bmatrix} F_{LRx} \\ F_{Ly} \\ F_{Ry} \\ F_{Lz} \\ F_{Rz} \\ F_{Tz} \end{Bmatrix}$$
$$= \begin{Bmatrix} -\sum F_{x_i} \\ -\sum F_{y_i} \\ -\sum F_{z_i} \\ \sum F_{y_i} D_{z_i} - \sum F_{z_i} D_{y_i} \\ \sum F_{z_i} D_{x_i} - \sum F_{x_i} D_{z_i} \\ \sum F_{x_i} D_{y_i} - \sum F_{y_i} D_{x_i} \end{Bmatrix} . \tag{A.4}$$

The L and R subscripts indicate left and right side of the TMJs. The T subscript indicates the tooth where bite force is exerted with x, y and z the components of a force. F indicates force while D is the distance in a specific coordinate direction from the occipital condyles average nodal coordinate (OC). The right hand side of the system is calculated as a summation of the muscle force and moment contribution about the OC location due to each muscle i.

The x-values of the force at each TMJ that makes up the bundled F_{LRx} is assumed to divide equally between the two. This gives a seventh equation $F_{Lx} = F_{Rx}$. These components of the force is assumed too small to affect the overall

results. A simple sensitivity analysis done for various ratio of x-component force proved that the final solution is fairly insensitive to this assumption.

The sensitivity analysis is done to compare the results of a finite element analysis for two scenarios. In the first scenario the force F_{LRx} is divided in such a way that 70% is attributed to the working side and 30% to the balancing side. The other analysis is done with the working side 30% and the balancing side 70%. Results of the FEA is visible in Figure A.2. A slight difference in stress field is visible at values far below the range intended for use to draw conclusions. This gives the impression that results obtained from an FEA on the skull is fairly insensitive to the assumption made on the seventh equation.

With no other constraints applied to the model the bite force on the tooth along with reaction forces at the articular eminances are expected to balance the system. Tables A.3 and A.4 contain all of the forces applicable to the two skull geometries including the reaction forces after solving the set of equations and dividing the bundled F_{LRx} equally between the working and balancing sides.

The forces applied and reaction forces obtained are visible in Figures A.3 - A.6. These figures show boundary conditions for the prognathic and orthognathic skull forms with the red lines indicating the muscle forces applied and the blue lines the reaction forces after solving the system of equations. The force values are scaled with 0.5 for visual clarity. Each muscle's contribution to the reaction forces is also illustrated. After obtaining the resultant forces, the orthognathic skull forces were scaled by 0.9412 for the molar bite and 0.9552 for the incisor bite analysis so the stress patterns for the same applied force at the tooth could be recovered and compared.

A.5 Analysis

Both skulls are treated similarly and several finite element analyses are run for incisal and molar bite using FEBio [3]. Muscle forces with their balancing reaction forces are applied as boundary conditions while the nodal coordinates of the occipital condyles at the foramen magnum are constrained. The use of a linear elastic skull model also allows the analysis of isolated muscle contributions to bite force and reaction forces at the temporomandibular joint.

The analyses run for both prognathic and orthognathic skull form include:

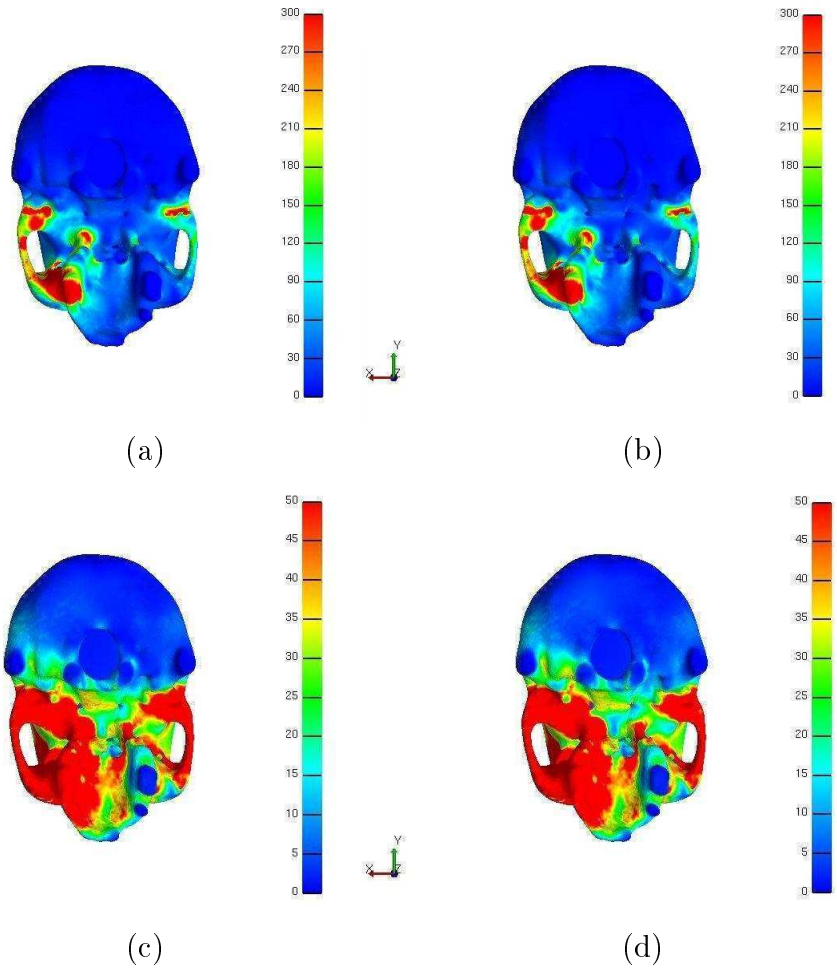

Figure A.2: Results of sensitivity analysis done on the orthognathic skull for a molar bite. This analysis was chosen because F_{LRx} is the largest in comparison to other resultant forces when an incisor bite or prognathic skull shape is considered. Working:balancing ratio of F_{LRx} left 1:$\frac{7}{3}$ and right $\frac{7}{3}$:1 for Von Mises stress set to a maximum of (a), (b) 300 N/cm^2 and (c), (d) 50 N/cm^2. Slight variation in stress field is only visible for stresses far below the range of stresses used in drawing conclusions from FEA results.

	Working Side		Balancing Side	
	Force [N]	**Direction**	**Force [N]**	**Direction**
Temporalis				
Section 1	183.54	{-0.055, 0.14, -0.989}	70.45	{0.039, 0.154, -0.987}
2	73.384	{-0.1, -0.149, -0.984}	36.66	{0.07, -0.144, -0.987}
3	52.42	{-0.138, -0.365, -0.921}	26.32	{0.116, -0.383, -0.916}
4	62.302	{-0.187, -0.582, -0.791}	23.04	{0.15, -0.582, -0.799}
5	32.95	{-0.196, -0.737, -0.647}	11.82	{0.157, -0.743, -0.65}
6	15.84	{-0.21, -0.829, -0.519}	6.94	{0.186, -0.839, -0.512}
7	27.52	{-0.235, -0.849, -0.473}	9.87	{0.241, -0.854, -0.461}
Masseter				
Superficial	230	{-0.09, 0.22, -0.971}	108.1	{0.09, 0.22, -0.971}
Deep Head	100	{-0.37, -0.13, -0.92}	36	{0.37, -0.13, -0.92}
Pterygoid				
Medial:	250	{0.469, 0.399, -0.788}	50	{-0.469, 0.399, -0.788}
	Reaction Forces			
Articular Eminance				
Molar Bite	358.11	{-0.034, -0.044, 0.998}	234.07	{-0.051, -0.08, 0.996}
Incisor Bite	635.65	{-0.019, -0.025, 0.999}	203.13	{-0.059, -0.092, 0.994}
Tooth				
Molar	657.23	{0,0,1}		
Incisor	410.55	{0,0,1}		

Table A.3: Prognathic force values and directions.

	Working Side		Balancing Side	
	Force [N]	**Direction**	**Force [N]**	**Direction**
Temporalis				
Section 1	178.05	{-0.068, 0.22, -0.973}	72.40	{0.094, 0.153, -0.984}
2	74.80	{-0.102, -0.095, -0.99}	30.75	{0.107, -0.123, -0.987}
3	69.19	{-0.121, -0.33, -0.936}	24.60	{0.116, -0.347, -0.931}
4	48.62	{-0.163, -0.551, -0.818}	24.11	{0.134, -0.562, -0.816}
5	32.32	{-0.187, -0.724, -0.664}	14.50	{0.13, -0.725, -0.676}
6	20.40	{-0.231, -0.821, -0.514}	7.46	{0.161, -0.826, -0.54}
7	27.82	{-0.301, -0.803, -0.523}	10.76	{0.234, -0.813, -0.533}
Masseter				
Superficial	230	{-0.07, 0.19, -0.979}	108.1	{0.07, 0.19, -0.979}
Deep Head	100	{-0.16, -0.19, -0.969}	36	{0.16, -0.19, -0.969}
Pterygoid				
Medial:	250	{0.65, 0.12, -0.75}	50	{-0.65, 0.12, -0.75}
	Reaction Forces			
Articular Eminance				
Molar Bite	344.28	{-0.113, 0.06, 0.992}	215.50	{-0.181, 0.116, 0.977}
Incisor Bite	643.28	{-0.061, 0.032, 0.998}	184.54	{-0.211, 0.136, 0.968}
Tooth				
Molar	698.29	{0,0,1}		
Incisor	429.78	{0,0,1}		

Table A.4: Orthognathic force values and directions.

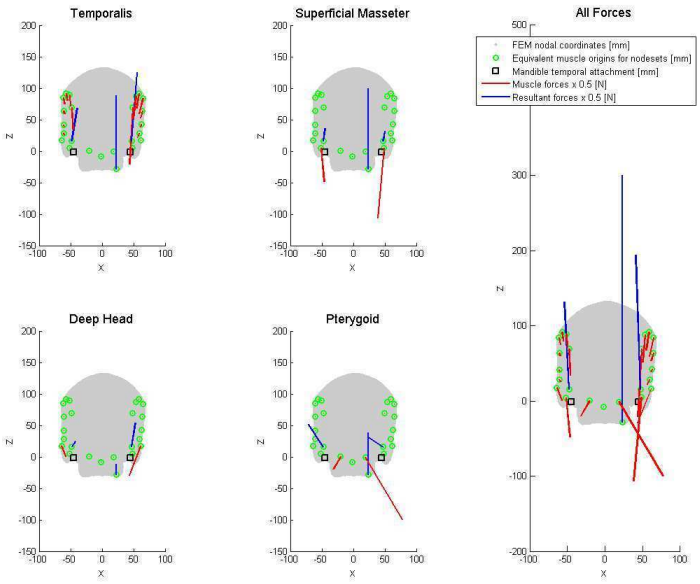

(a)

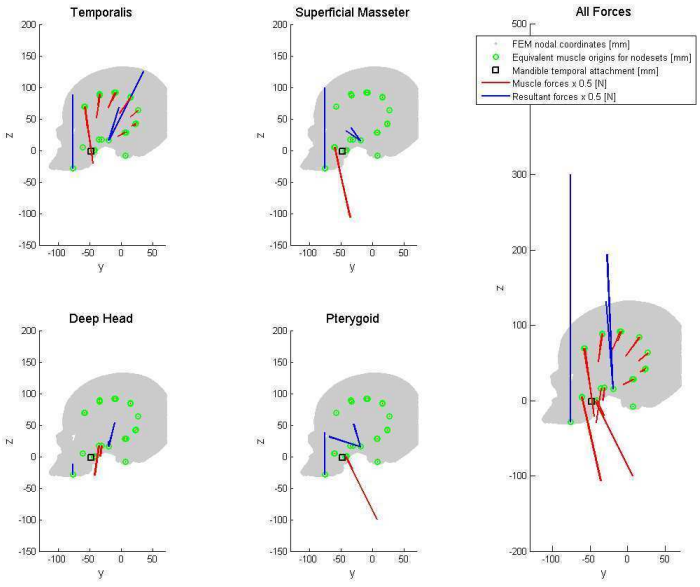

(b)

Figure A.3: Muscle contribution and reaction forces on the prognathic skull for a vertical molar bite.

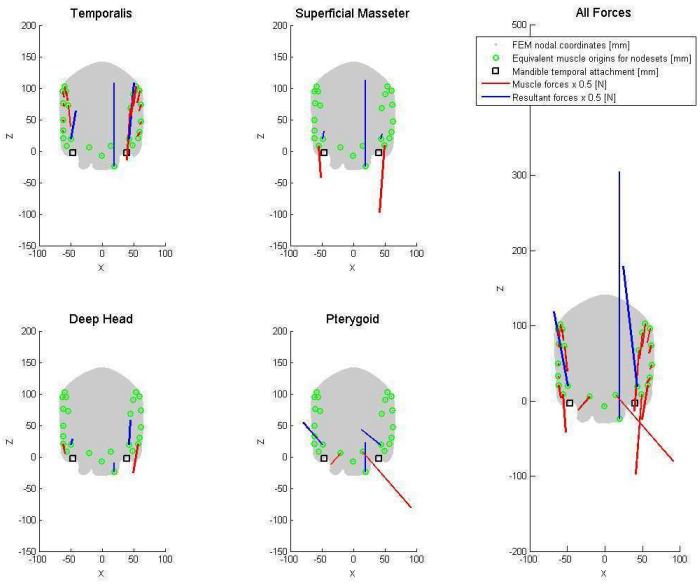

(a)

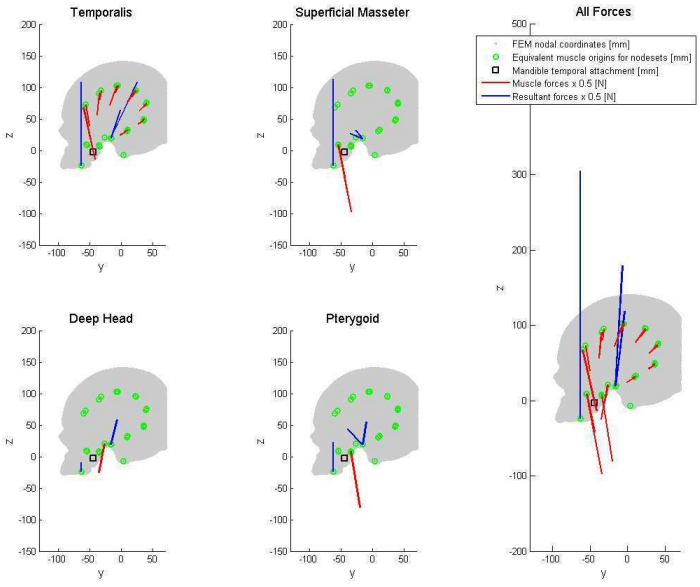

(b)

Figure A.4: Muscle contribution and reaction forces on the orthognathic skull for a vertical molar bite.

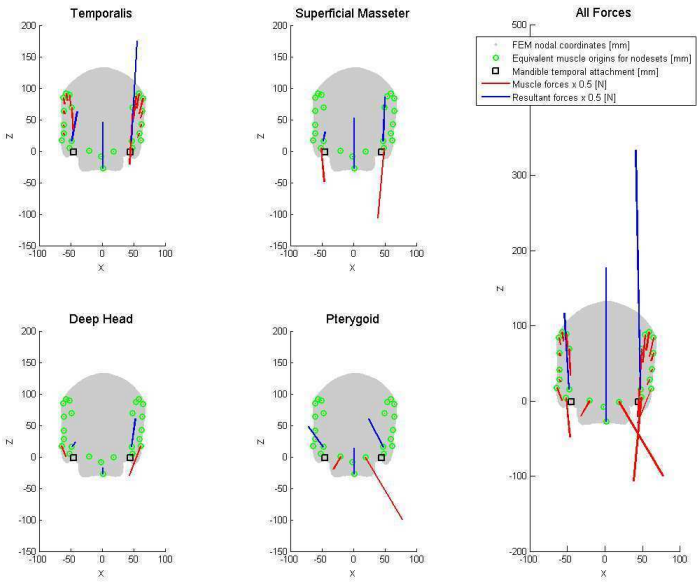

(a)

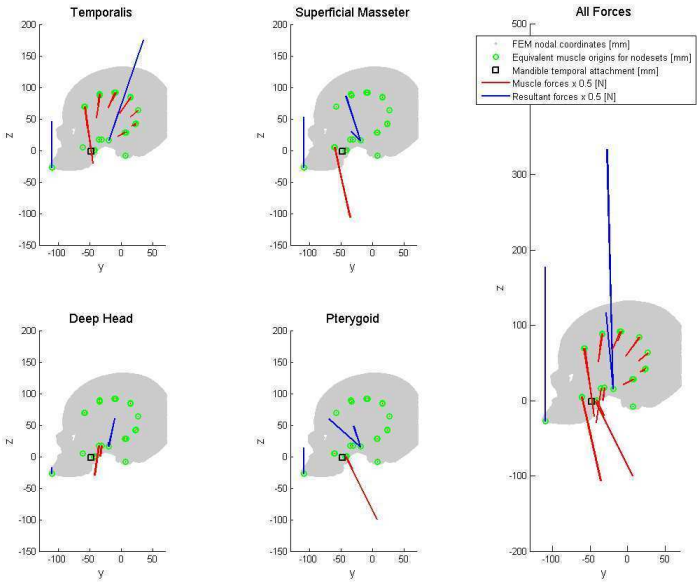

(b)

Figure A.5: Muscle contribution and reaction forces on the prognathic skull for a vertical incisor bite.

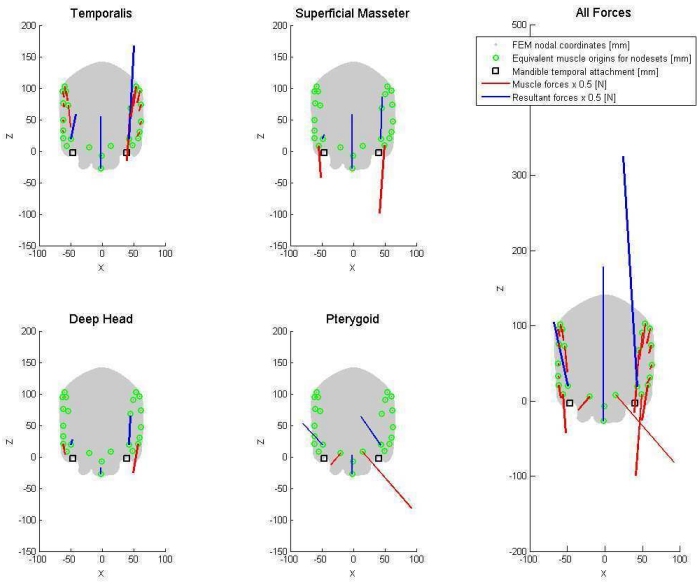

(a)

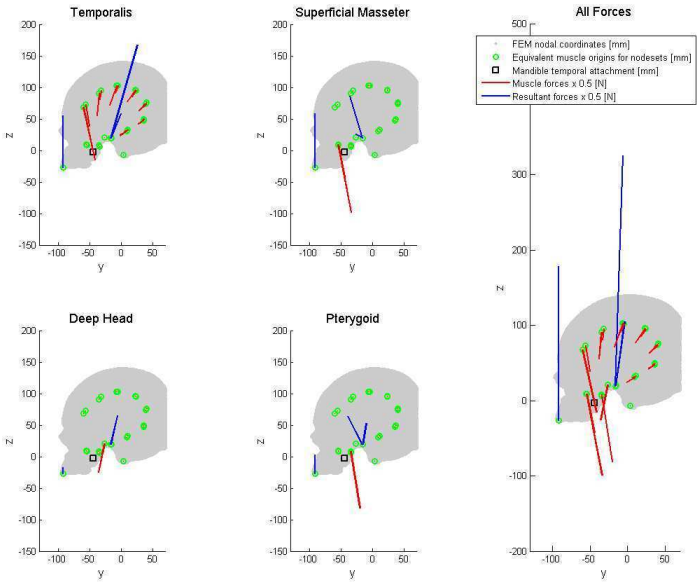

(b)

Figure A.6: Muscle contribution and reaction forces on the orthognathic skull for a vertical incisor bite.

- The effect of the Temporalis muscle on molar and incisor bite.
- The effect of the Superficial Masseter on molar and incisor bite.
- The effect of the Deep head Masseter on molar and incisor bite.
- The effect of the Medial Pterygoid on molar and incisor bite.
- The effect of all muscle contributions on molar and incisor bite.

This results in a total of 20 analyses done on masticatory induced stress. Post processing and visualisation is done using PostView [6]. Principal stresses, displacements and Von Mises stresses are considered to generate stress state and displacement plots.

Working side stresses are visible in Figures A.7 and A.8 for the full molar and incisor bite simulations. Muscle contribution to the prognathic and orthognathic molar bite Von Mises stress is presented as an example in Figure A.9.

A.6 Results

The displacement results for the full analysis on both skull forms for first molar and first incisor bite are documented in Table A.5. Here the displacements on the prognathic skull are greater than the displacements on the orthognathic form.

The maximum Von Mises stresses for all 20 analyses are given in Table A.6. Comparing these maximums for various muscle contributions, the same analysis for the different geometries occasionally differ by a factor 2. The significance thereof is doubtful as there is no guarantee that the higher stress is not caused by singularities. These singularities could occur due to unsmoothed areas, inadequate element quality and stiffness or greater point loads.

The analysis done for incisal bite on the orthognathic and molar bite on the prognathic skull shape are displayed in Figure A.10. Only the lower view of these analyses is given along with detail to indicate that the maximum Von Mises stresses do indeed occur at singular locations. In Figure A.10 (a) and (c) the stress concentration is due to the discretisation of the shape in such a way that point loads are applied in the region of the TMJ while the stress concentrations in Figure A.10 (b) and (d) seem to occur at holes in the geometry. These holes in the prognathic shape are not present in the orthognathic shape which means that the difference in

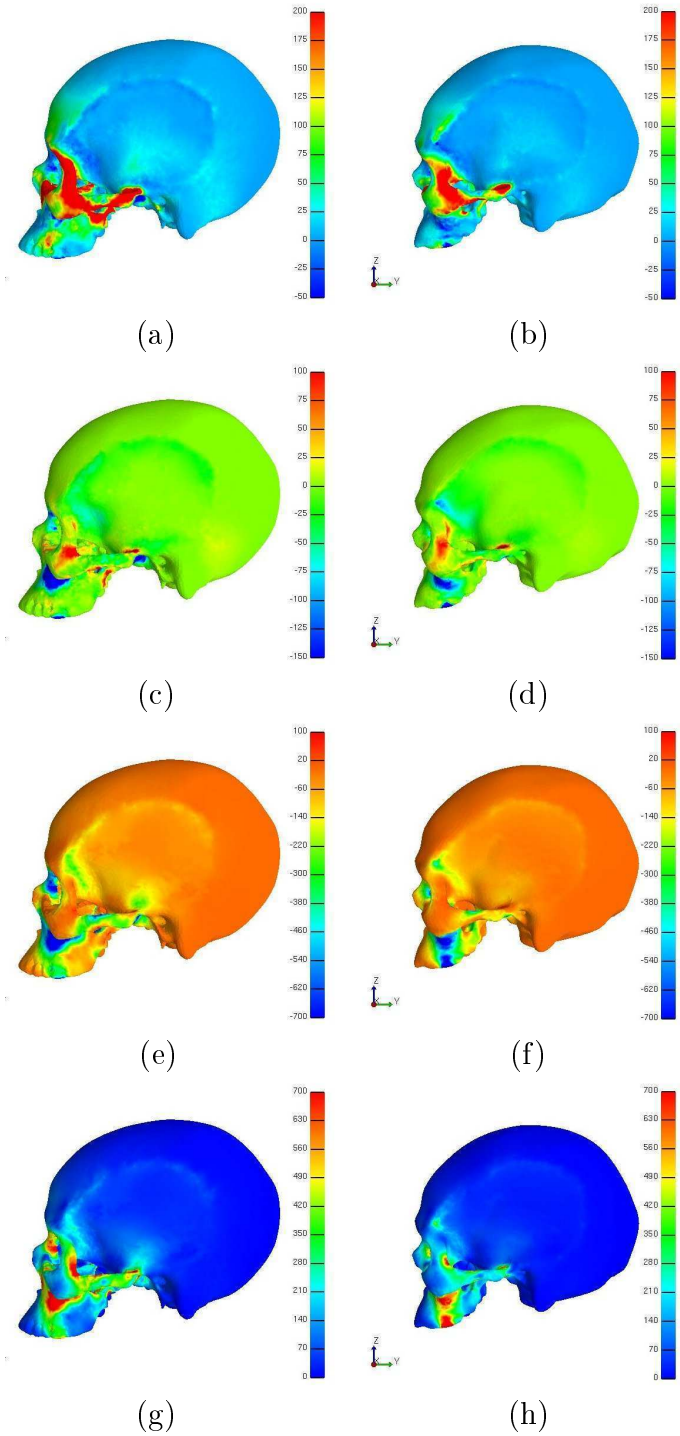

Figure A.7: Lateral view of the working side stresses for a molar bite on full prognathic and orthognathic FEA results in N/cm^2. (a), (b) 1st principal stress (c), (d) 2nd principal stress (e), (f) 3rd principal stress and (g), (h) Von Mises stress.

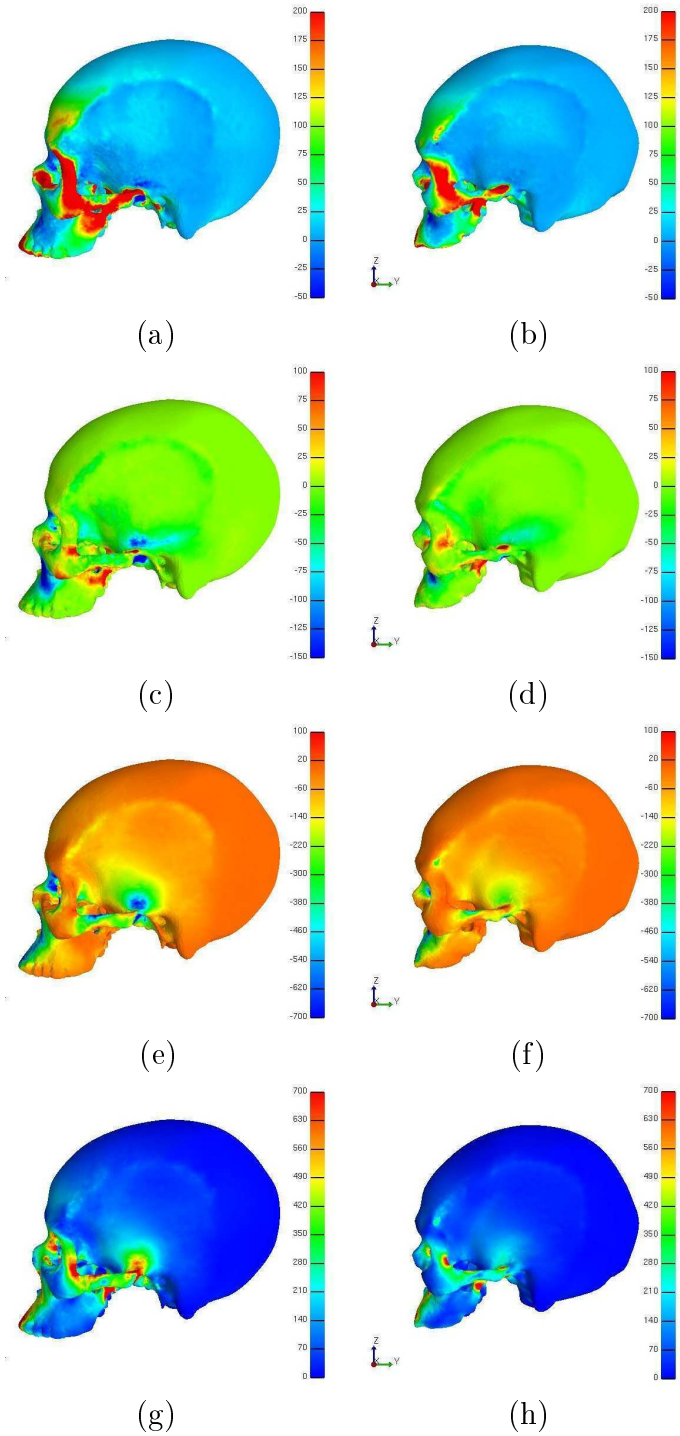

Figure A.8: Lateral view of the working side stresses for incisor bite on full prognathic and orthognathic FEA results in N/cm^2. (a), (b) 1st principal stress (c), (d) 2nd principal stress (e), (f) 3rd principal stress and (g), (h) Von Mises stress.

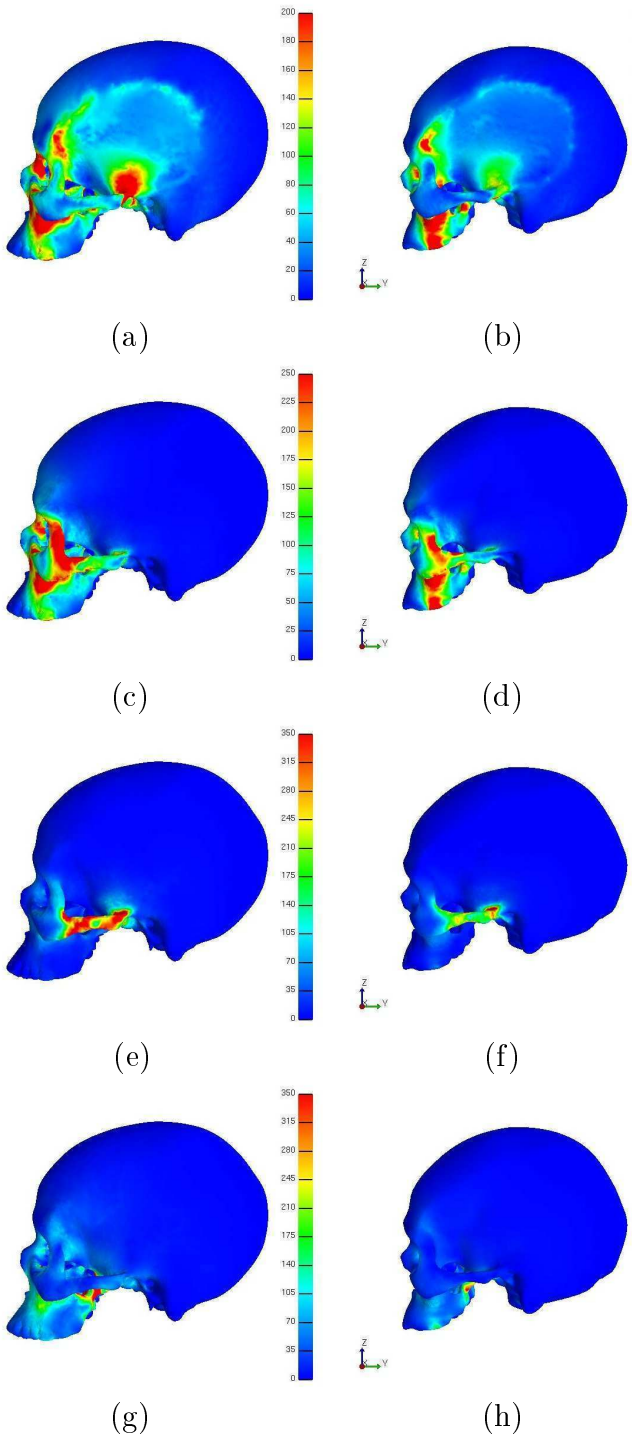

Figure A.9: Lateral view of the working side muscle contribution to Von Mises stress. The molar bite for prognathic and orthognathic FEA results are given in N/cm^2. (a), (b) Temporalis (c), (d) superficial masseter (e), (f) deep head masseter and (g), (h) medial pterygoid contributions.

	Prognathic		Orthognathic	
	Min [mm]	Max [mm]	Min [mm]	Max [mm]
	Molar Bite			
x	-1.07E-02	2.65E-02	-3.88E-03	1.32E-02
y	-1.80E-02	7.51E-03	-7.34E-03	3.87E-03
z	-3.03E-02	2.63E-02	-1.81E-02	1.56E-02
Total	0	3.99E-02	0	2.08E-02
	Incisor Bite			
x	-8.66E-03	9.82E-03	-5.91E-03	6.45E-03
y	-5.21E-02	1.25E-02	-4.08E-02	6.27E-03
z	-2.00E-02	8.51E-02	-1.59E-02	4.61E-02
Total	0	9.72E-02	0	6.11E-02

Table A.5: Minimum and maximum displacements obtained from finite element analysis for all mastication forces.

	Molar Results [MPa]		**Incisor Results** [MPa]	
	Prognathic	Orthognathic	Prognathic	Orthognathic
Temporalis	7.12	16.45	10.85	24.58
Superficial M	8.35	7.34	11.85	10.16
Deep Head M	7.51	6.77	7.40	7.70
Pterygoid	15.42	8.89	15.10	9.64
All Muscles	14.72	24.65	30.49	45.52

Table A.6: Maximum Von Mises stress obtained from finite element analysis for individual mastication forces and full analysis.

maximum Von Mises stress reported in Table A.6 could also be due to topological inconsistency between the skull geometries.

It is noted from the initial analysis that the skull geometries vary in more ways than just prognathism. These variations seem to play a significant role in the stresses that are reported and further attention should be given to the similarities and differences of the skull forms represented.

When the skull computational domains vary in only their relative degree in prognathism, a conclusion may be drawn on the effect of prognathism on masticatory induced stress.

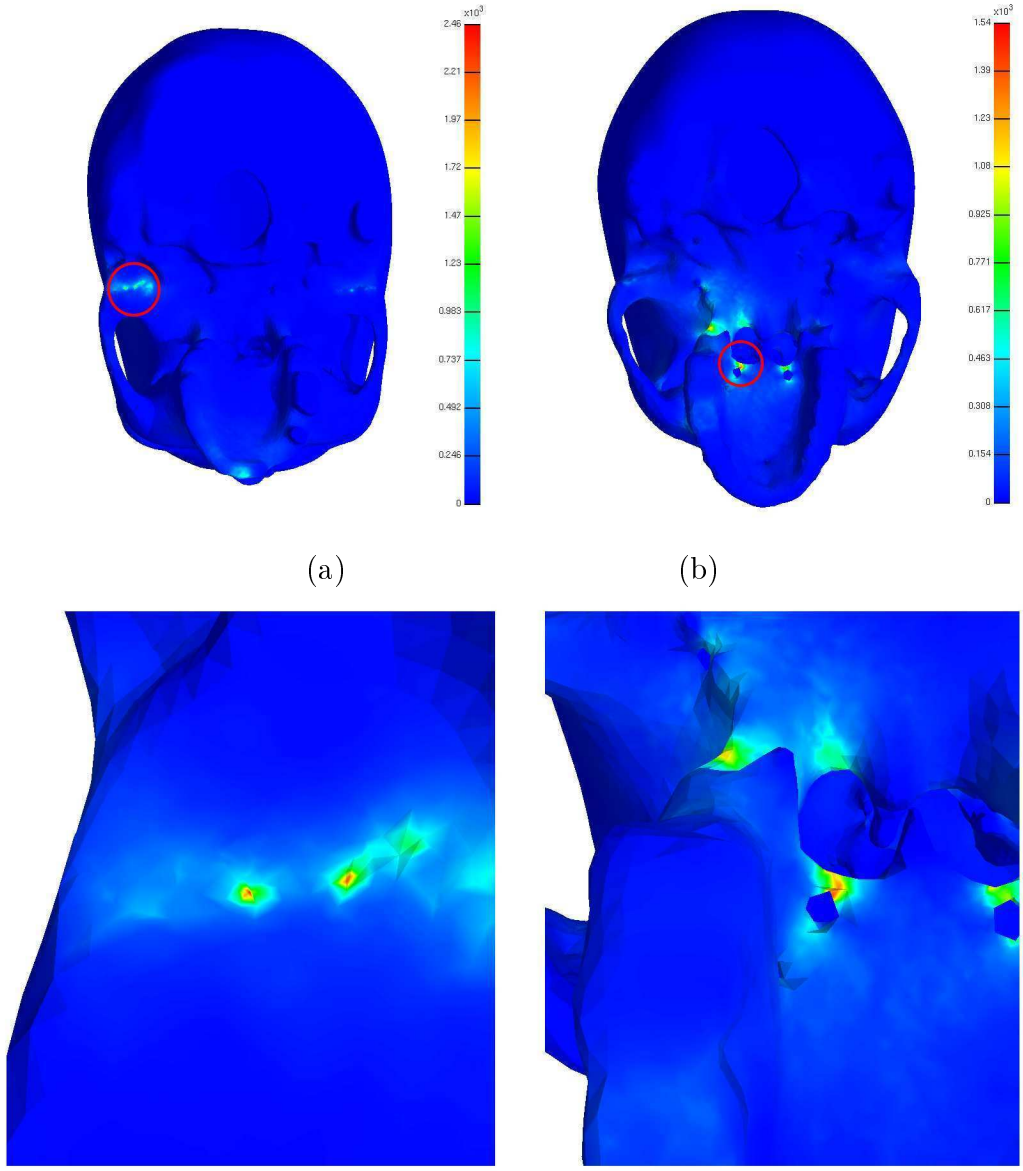

(a) (b)

(c) (d)

Figure A.10: Von Mises stress concentrations. (a) Lower view of the incisal bite analysis on the orthognathic skull geometry with detail in (c). (b) Lower view of the molar bite analysis on the prognathic skull geometry with detail in (d). Stress concentrations in these two analyses are shown with reference to Table A.6. Maximum Von Mises stress occurs at stress concentrations and can not be compared.

Appendix B

Affine Iterative Closest Point Problem

B.1 Reformulating the ICP problem

Reformulating the Iterative Closest Point algorithm mentioned in subsection 3.1.1 is done as in the work by Du *et al.* [28]. First assume that an affine transformation is to be applied to one point set. This is done in such a way that it matches a subset of another point set. The problem is still to find an affine transformation T that best aligns $\mathcal{P}$ to $\mathcal{M}$:

$$\min_{T,j\in\{1,2,\ldots,N_m\}} \left(\sum_{i=1}^{N_p} \|T(\mathbf{p}_i) - \mathbf{m}_j\|_2^2 \right). \tag{B.1}$$

This affine transformation is expressed explicitly as an invertible matrix $\mathbf{A}$ and translation vector $\mathbf{t}$ so that the problem is again expressed as in Equation (3.2). Using Singular Value Decomposition (SVD), the invertible matrix can be decomposed into two orthogonal matrices $\mathbf{U}$ and $\mathbf{V}$, as well as a positive diagonal matrix $\mathbf{S}$ so that $\mathbf{A} = \mathbf{USV}^T$. It is assumed that $\mathbf{R}$ is the orthogonal rotation matrix $\mathbf{V}^T$.

The affine transformation problem is rewritten in such a way that T is represented by the orthogonal reflection and rotation matrices $\mathbf{U}$ and $\mathbf{R}$, with a scale transformation $\mathbf{S}$, and a translation $\mathbf{t}$.

The problem set up in Equation (B.1) now takes the form

$$\min_{\mathbf{U},\mathbf{S},\mathbf{R},\mathbf{t},j\in\{1,2,\ldots,N_m\}} \left(\sum_{i=1}^{N_p} \|\mathbf{USRp}_i + \mathbf{t} - \mathbf{m}_j\|_2^2\right), \tag{B.2}$$

such that:

$$\mathbf{U}^T\mathbf{U} = \mathbf{I}_m, \quad \det(\mathbf{U}) = 1, \tag{B.3}$$

$$\mathbf{R}^T\mathbf{R} = \mathbf{I}_m, \quad \det(\mathbf{R}) = 1,$$

$$\mathbf{S} = \operatorname{diag}(s_1, s_2, \ldots, s_m), \quad s_j \in [a_j, b_j].$$

where a_j and b_j are the upper and lower bounds of the allowable scale transformation.

This reformulated problem is then iteratively performed in much the same way as the original ICP but with reflection, rotation, scale and translation instead of only rotation and translation.

B.2 Lie group and lie algebra

A set of mappings on a differential manifold is defined as a lie group [28]. A rotation in $\mathbb{R}^m$ can be expressed by a set of $m \times m$ special orthogonal matrices. This matrix is represented as the special orthogonal group

$$SO(m) = \left\{\mathbf{R} \in \mathbb{R}^{m\times m} | \mathbf{R}^T\mathbf{R} = \mathbf{I}_m, \det(\mathbf{R}) = 1\right\}. \tag{B.4}$$

This group then has a linearised form or lie algebra

$$\mathfrak{so}(m) = \left\{\mathbf{R} \in \mathbb{R}^{m\times m} | \mathbf{R} = -\mathbf{R}^T\right\} \tag{B.5}$$

which is an $N_r := m(m-1)/2$ dimensional linear space. The rotation matrix $\mathbf{R}$ can be expressed as

$$\mathbf{R} = \sum_{i=1}^{N_r} x_i \mathbf{E}_i, \tag{B.6}$$

where x_i and $\mathbf{E}_i$ is the first canonical coordinate and basis of $\mathfrak{so}(m)$. The basis in

two dimensions is denoted by

$$\mathbf{E}_1 = \begin{bmatrix} 0 & 1 \\ -1 & 0 \end{bmatrix} \tag{B.7}$$

and in three dimensions, the basis of $\mathfrak{so}(3)$ is

$$\mathbf{E}_1 = \begin{bmatrix} 0 & 1 & 0 \\ -1 & 0 & 0 \\ 0 & 0 & 0 \end{bmatrix}, \quad \mathbf{E}_2 = \begin{bmatrix} 0 & 0 & 0 \\ 0 & 0 & -1 \\ 0 & 1 & 0 \end{bmatrix}, \quad \mathbf{E}_3 = \begin{bmatrix} 0 & 0 & 1 \\ 0 & 0 & 0 \\ -1 & 0 & 0 \end{bmatrix}. \tag{B.8}$$

A lie group and its lie algebra are related by an exponential mapping. Given an element $\mathbf{B}$ in a certain neighbourhood of $\mathbf{A}$ in $SO(m)$, a unique $\mathbf{Q} \in \mathfrak{so}(m)$ exists such that there is a smooth exponential mapping between them

$$\mathbf{B} = \mathbf{A}e^{\mathbf{Q}}. \tag{B.9}$$

B.3 Performing an Affine ICP transformation

As with the ICP method, the first step to performing a k^{th} affine transformation is setting up a point correspondence. This is done using a $k-d$ tree representation of the model shape $\mathcal{M}$ for nearest neighbour search. The implementation is done in python using `scipy.spatial` [11]. The correspondence is set up with the $(k-1)^{\text{th}}$ transformations as

$$c_k(i) = \underset{j \in \{1,2,\ldots,N_m\}}{\arg\min} \left(\|(\mathbf{U}_{k-1}\mathbf{S}_{k-1}\mathbf{R}_{k-1}\mathbf{p}_i + \mathbf{t}_{k-1}) - \mathbf{m}_j\|_2^2 \right), \quad i = 1, 2, \ldots, N_p. \tag{B.10}$$

The optimisation problem posed in Equation (B.2) is simplified using exponential mappings of lie group and their Taylor approximations at each iteration [28]. This is done assuming the change in transformation is small between consecutive iterations such that $\mathbf{U}_k$ is in the neighbourhood of $\mathbf{U}_{k-1}$ for example, allowing the use of exponential mapping.

After setting up a point correspondence, the translation required for a minimum

value of the cost function in Equation (B.2) can be calculated as [28]

$$\mathbf{t}_k = \frac{1}{N_p}\sum_{i=1}^{N_p}\mathbf{m}_{c_k(i)} - \frac{1}{N_p}\sum_{i=1}^{N_p}\mathbf{U}_{k-1}\mathbf{S}_{k-1}\mathbf{R}_{k-1}\mathbf{p}_i \tag{B.11}$$

where $\mathbf{m}_{c_k(i)}$ is the closest point on $\mathcal{M}$ for $\mathbf{p}_i$ on $\mathcal{P}$.

Taking this known translation into account, the objective function is rewritten. If

$$\mathbf{p}_{\mathbf{t}i} \triangleq \mathbf{p}_i - \frac{1}{N_p}\sum_{i=1}^{N_p}\mathbf{p}_i, \quad \mathbf{m}_{\mathbf{t}i} \triangleq \mathbf{m}_{c_k(i)} - \frac{1}{N_p}\sum_{i=1}^{N_p}\mathbf{m}_{c_k(i)}, \tag{B.12}$$

the objective function can be rewritten as

$$\min_{\mathbf{U},\mathbf{S},\mathbf{R},\mathbf{t},j\in\{1,2,\ldots,N_m\}} \left(\sum_{i=1}^{N_p}\|\mathbf{USR}\mathbf{p}_{\mathbf{t}i} - \mathbf{m}_{\mathbf{t}i}\|_2^2\right). \tag{B.13}$$

Because each k^{th} transformation matrix is in the neighbourhood of the previous, the lie group and lie algebra allow updating them at each iteration as in Equation (B.9):

$$\begin{aligned}\mathbf{U}_k &= \mathbf{U}_{k-1}e^{\sum_{j=1}^{N_r} u_j\mathbf{E}_j}, \\ \mathbf{R}_k &= \mathbf{R}_{k-1}e^{\sum_{j=1}^{N_r} r_j\mathbf{E}_j},\end{aligned} \tag{B.14}$$

where $N_r := m\,(m-1)\,/2$ for a problem in $\mathbb{R}^m$.

The scale matrix is also updated using a smooth exponential mapping. This smooth mapping may be expressed as

$$\mathbf{S}_k = \mathbf{S}_{k-1}e^{\sum_{j=1}^{N_s} s_j\mathbf{D}_j},$$

where $\mathbf{D}_j$ is the set of the bases of a diagonal matrix with only $D_{jj} = 1$ and $N_s := m$ for a problem in $\mathbb{R}^m$.

If the change in transformation is not large, the Taylor series of the exponential mappings are guaranteed to converge and are rewritten with the higher order terms omitted [28]. This results in the k^{th} iteration constrained optimisation problem

written in the form

$$\min_{\mathbf{c}} \quad \sum_{i=1}^{N_p} \left\| \mathbf{U}_{k-1} \left(\mathbf{I} + \sum_{j=1}^{N_r} u_j \mathbf{E}_j \right) \mathbf{S}_{k-1} \left(\mathbf{I} + \sum_{j=1}^{N_s} s_j \mathbf{D}_j \right) \times \mathbf{R}_{k-1} \left(\mathbf{I} + \sum_{j=1}^{N_r} r_j \mathbf{E}_j \right) \mathbf{p}_{\mathbf{t}i} - \mathbf{m}_{\mathbf{t}i} \right\|_2^2 \tag{B.15}$$

with $\mathbf{c} \triangleq \{u_1, ..., u_{N_r}, s_1, ..., s_{N_s}, r_1, ..., r_{N_r}\}^T$, consisting of N_r reflection, N_s scale and N_r rotation variables, to be determined. The scale constraints are updated at each iteration using the initial boundaries a_j and b_j and the previous scale matrix:

$$\sum_{j=1}^{N_s} s_j \mathbf{D}_j \in \left[\ln \left(\mathbf{S}_{K-1}^{-1} \text{diag}(a_1, ..., a_{N_s}) \right), \ \ln \left(\mathbf{S}_{K-1}^{-1} \text{diag}(b_1, ..., b_{N_s}) \right) \right]. \tag{B.16}$$

Appendix C

Shape Context Correspondence

Methods have been developed to classify feature points within the context of shape. These shape contexts can then be used to create point correspondences for use in registration.

Given a set of points on a surface, a 3D shape context for each point can provide the approximate corresponding point locations on a target surface with a similar shape. Once a matching is established, the base surface can be warped to represent the target with a smooth deformation model such as a thin plate spline (TPS) radial basis function (RBF).

A limiting factor of using shape context for point matching is the significant amount of mismatched points that may occur between two objects because of global and local dissimilarity and the existence of outliers [68]. This is classically improved by the straightforward removal of a percentage of correspondences with the highest cost. This is done with the assumption that a mismatched point correspondence would have a greater difference between the initial and registered coordinate position than a trusted registration.

The method for setting up point correspondences for shape context non-rigid registration is described in this section and accompanied by figures and results found in literature.

C.1 Shape Context

The shape context of a point is a measure of the distribution of relative positions of neighbouring points [68]. This distribution is defined as a joint histogram where

each axis represents a parameter in a polar coordinate system. In two dimensions, a 2D log-polar histogram is set up as in the template given in Figure C.1 (a). This can also be extended to 3D using the spherical coordinates of Figure C.1 (b).

To set up a shape context histogram, the user specifies the number of bins to use. The support region is divided into bins by equally spaced boundaries in the azimuth and elevation dimensions with logarithmically spaced boundaries along the radial dimension. Sampling logarithmically makes the descriptor more robust to distortions in shape further from the basis point [31]. With the number of radial bins J, a minimum radius $r_{\min}$ and maximum radius $r_{\max}$ specified, the $J+1$ radius boundaries are calculated as [31]

$$R_j = \mathrm{e}^{\ln(r_{\min})+\frac{j}{J}\ln(r_{\max}/r_{\min})}. \tag{C.1}$$

A shape context histogram is set up with the points within a spherical radius of $r_{\max}$ of the point under consideration. The contribution to the bin count for a point p_i is given by

$$\omega_i = \frac{1}{\rho_i \sqrt[3]{V_i\left(j,k,l\right)}} \tag{C.2}$$

where $V_i\left(j,k,l\right)$ is the volume of the bin at the j^{th} radial, k^{th} elevation and l^{th} azimuth that contains point p_i. ρ_i is the local point density around the bin [31]. Normalising in this way takes the large variation in bin size with radius and elevation into account. The local point density ρ_i is simply estimated as the count of points in a sphere of radius δ around p_i.

The example of matching and registering two elephant outlines using shape context is presented with the aid of Figures C.2 and C.3. After setting up the histograms of feature points A to D in these figures for example, a measure of similarity between two shape context can be computed as a cost between the two histograms. This is done by using the χ^2-distance [22, 68, 69]:

$$C_{mn} = \frac{1}{2}\sum_{i=1}^{N_b}\frac{\left(h_m\left(i\right)-h_n\left(i\right)\right)^2}{h_m\left(i\right)+h_n\left(i\right)} \tag{C.3}$$

with h_m and h_n the shape context histograms of the points m and n having the bins $i = 1, 2, ..., N_b$. In this equation, C_{mn} is the associated cost of matching points m and n where a low cost value by this definition translates into a high similarity between the two points.

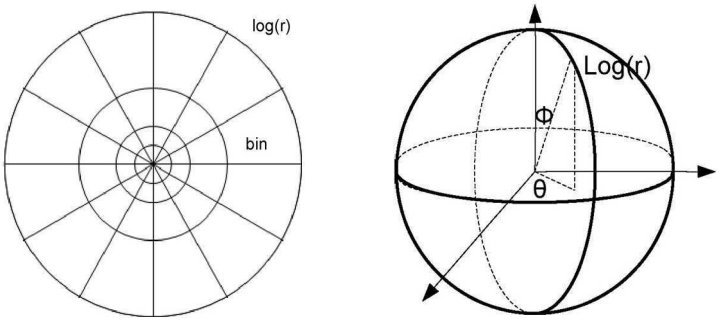

(a) (b)

Figure C.1: a) 2D log-polar histogram bins for 2D shape context. b) 3D spherical coordinates for use in setting up 3D shape context histogram. [68]

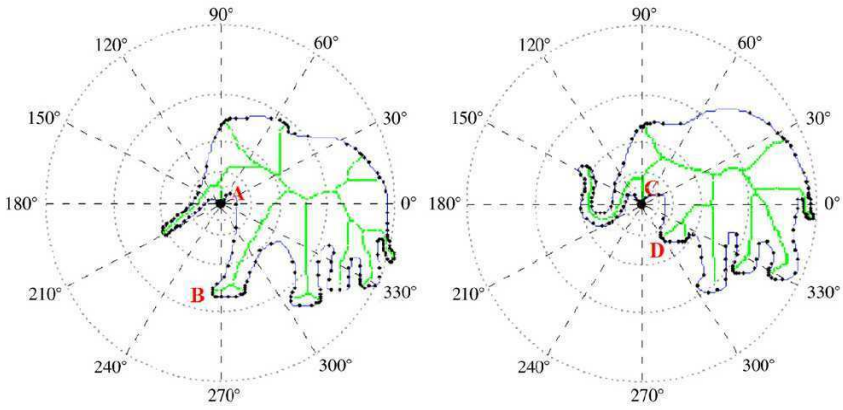

(a) (b)

Figure C.2: Shape context after first creating skeletal lines. This is done here by Xie *et al.* [69] for two different elephant outlines. The images illustrate the image position for setting up a shape context histogram for points A in (a) and C in (b).

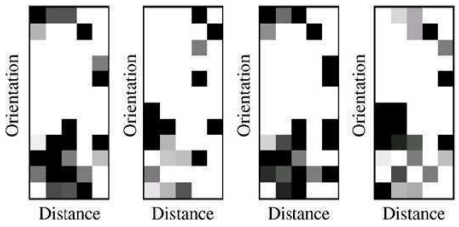

(a) (b) (c) (d)

Figure C.3: Shape context histograms of the four points a) A, b) B, c) C and d) D marked in Figure C.2 [69]. Here the corresponding points are seen to have similar histograms if (a) and (c) are compared for example.

C.2 Point Matching

In performing registration, the shape context local feature comparison is done on point sets from two similar surfaces.

A cost matrix is set up between the two shapes with the number of rows equal to the number of points of shape one and the number of columns the same as the number of points in shape two for example. Each value in the matrix is the associated cost of similarity between the points represented by the specific row and column as expressed in Equation (C.3).

An ideal set of correspondences are the set of points in shape 1 that best resemble the associated set of points in shape 2. The goal is to find the matched points resulting in lowest total registration cost. This is represented as a bipartite matching problem and can be solved using various techniques [34]. Techniques such as the Hungarian method used in Xiao *et al.* [68] guarantees a number of matched point pairs equal to the number of points in the smaller point set. The spare points from the larger point set without matched points are discarded.

After completing the search, a fixed percentage of correspondences with low cost are traditionally selected as the point sets with high confidence. The matches with highest cost are discarded and the rest used to determine and apply a deformation.

Appendix D

Feature Registration on Dolphin Geometries

The performance of the implemented feature registration procedure is illustrated using two dolphin geometries. The two original geometries is obtained from the INRIA model shape repository [4]. One of the geometries is then refined, manipulated and smoothed to generate the target geometry in the feature registration example. The other geometry is only refined and smoothed.

Crest lines on the two geometries is extracted and thresholded to get rid of less significant lines. The target geometry and it's crest lines are displayed in Figure D.1. In this figure the lines on the generic dolphin shape are displayed in their original position.

A rigid registration is performed on the target geometry allowing isotropic scale with upper and lower constraints arbitrarily set as 0.5 and 1.5. The results of the isotropic scale ICP registration is displayed in Figure D.2. After rigid registration, the feature line registration procedure is implemented to deform the lines on the generic dolphin geometry to better represent that of the target. Resulting registered and deformed lines are visible in Figure D.3. Only the registered lines with a matched point portion of at least 50% is used and displayed.

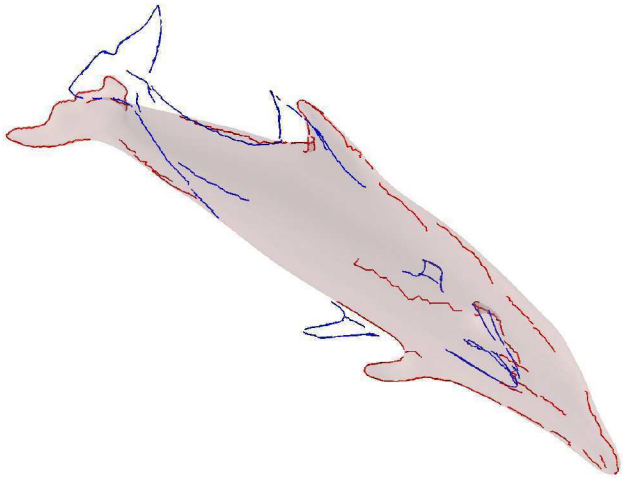

(a)

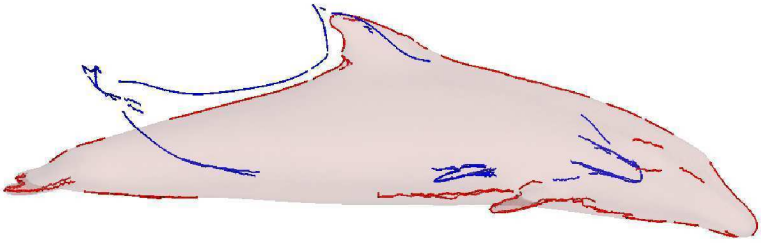

(b)

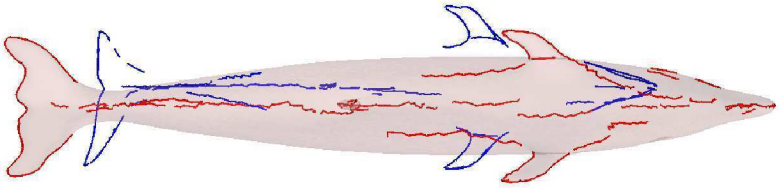

(c)

Figure D.1: Original position of a target and base dolphin geometry. The target geometry is illustrated in its original position with the target features in red and the base geometry features in blue. (a) Isometric, (b) lateral and (c) lower view.

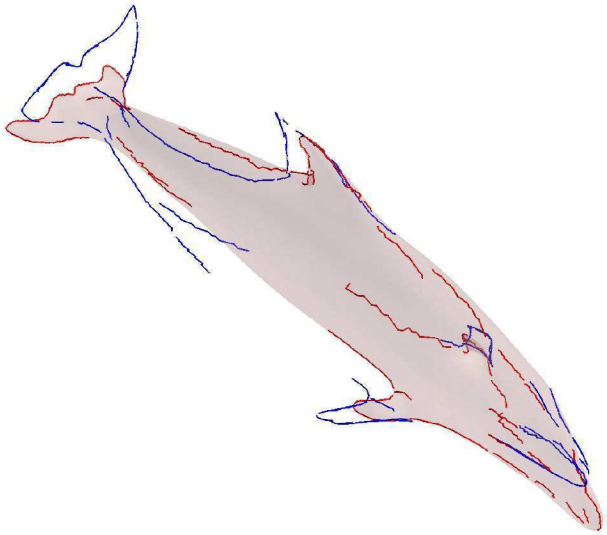

(a)

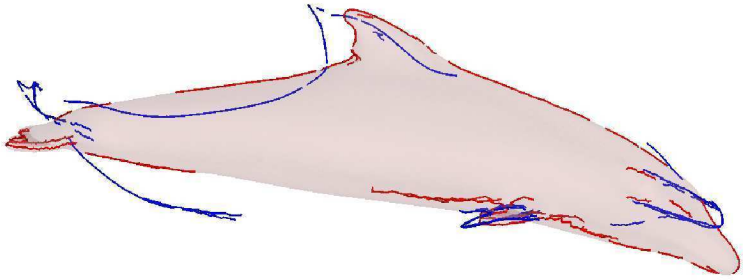

(b)

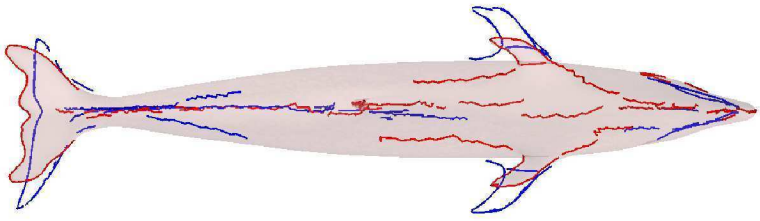

(c)

Figure D.2: Position of a target dolphin geometry relative to the base shape after isotropic scale ICP registration. The target geometry is illustrated in its registered position with the target features in red and the base geometry features in blue. (a) Isometric, (b) lateral and (c) lower view.

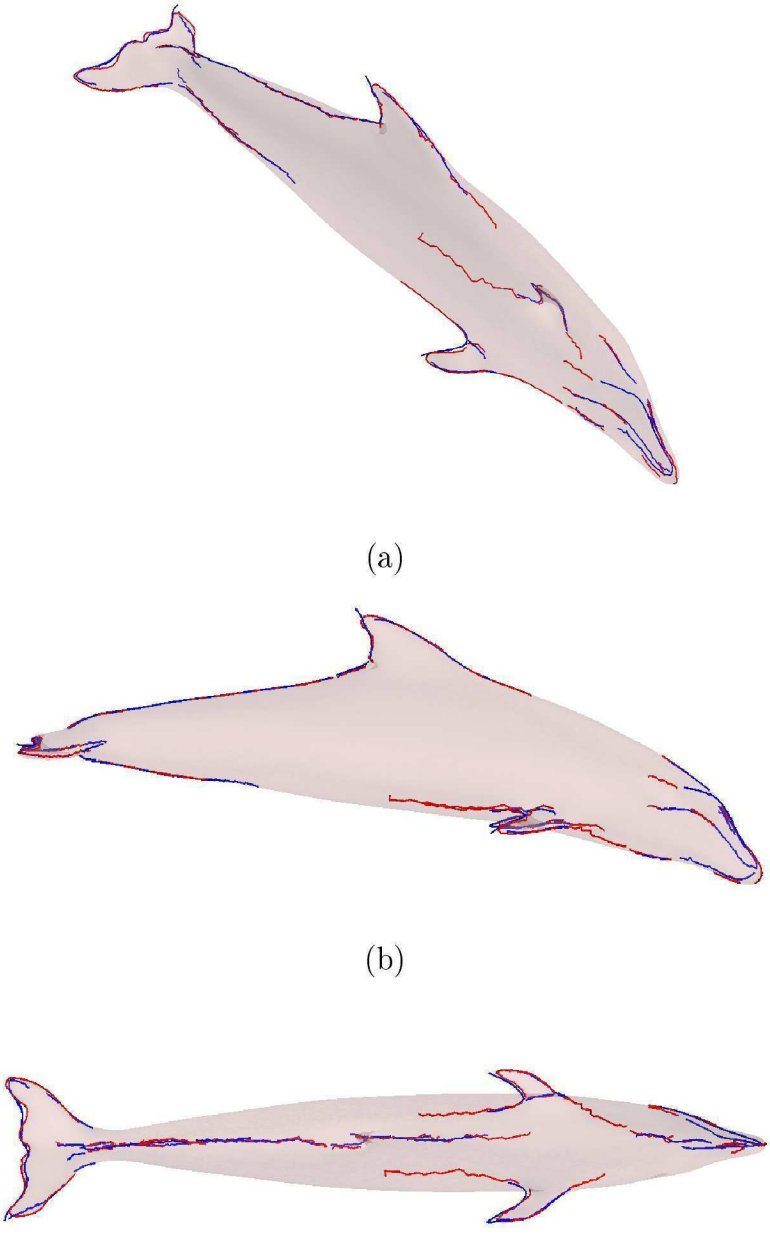

(a)

(b)

(c)

Figure D.3: Feature registration of a base dolphin to the aligned target configuration. The target geometry is illustrated in its aligned position with the target features in red and the deformed base geometry features in blue. Only the registered feature lines on both geometries are shown. (a) Isometric, (b) lateral and (c) lower view.